Supporting Information for

Thermomechanical Response of Supported Hexagonal Boron Nitride Sheets of Various Thicknesses

Lambros Seremetis[†, ‡], Emmanuel N. Koukaras[‡, £], Sotiria Alexandri[‡], Antonis Michail[†, ‡] George Kalosakas[¥], John Parthenios[‡], Costas Galiotis[‡, §] Sotirios Tsirkas[#], Spyridon Grammatikopoulos[‡, #] and Konstantinos Papagelis[, ‡, &]*

[†]Department of Physics, University of Patras, Patras, Patras, 26504 Greece

[‡]Institute of Chemical Engineering Sciences, Foundation of Research and Technology-Hellas (FORTH/ICE-HT), Stadiou Street, Platani, Patras, 26504 Greece

[£]Laboratory of Quantum and Computational Chemistry, Department of Chemistry, Aristotle University of Thessaloniki, GR-54124 Thessaloniki, Greece

[¥]Department of Materials Science, University of Patras, Patras, 26504 Greece

[§]Department of Chemical Engineering, University of Patras, Patras 26504 Greece

[#]Department of Mechanical Engineering, School of Engineering, University of the Peloponnese Megalou Alexandrou 1, 26334 Patras, Greece

[&]School of Physics, Department of Solid State Physics, Aristotle University of Thessaloniki, Thessaloniki 54124, Greece

* Corresponding Author: kpapag@physics.auth.gr

Contents

1. Raman spectra of monolayer *h*BN in the E_{2g} band frequency region at various temperatures

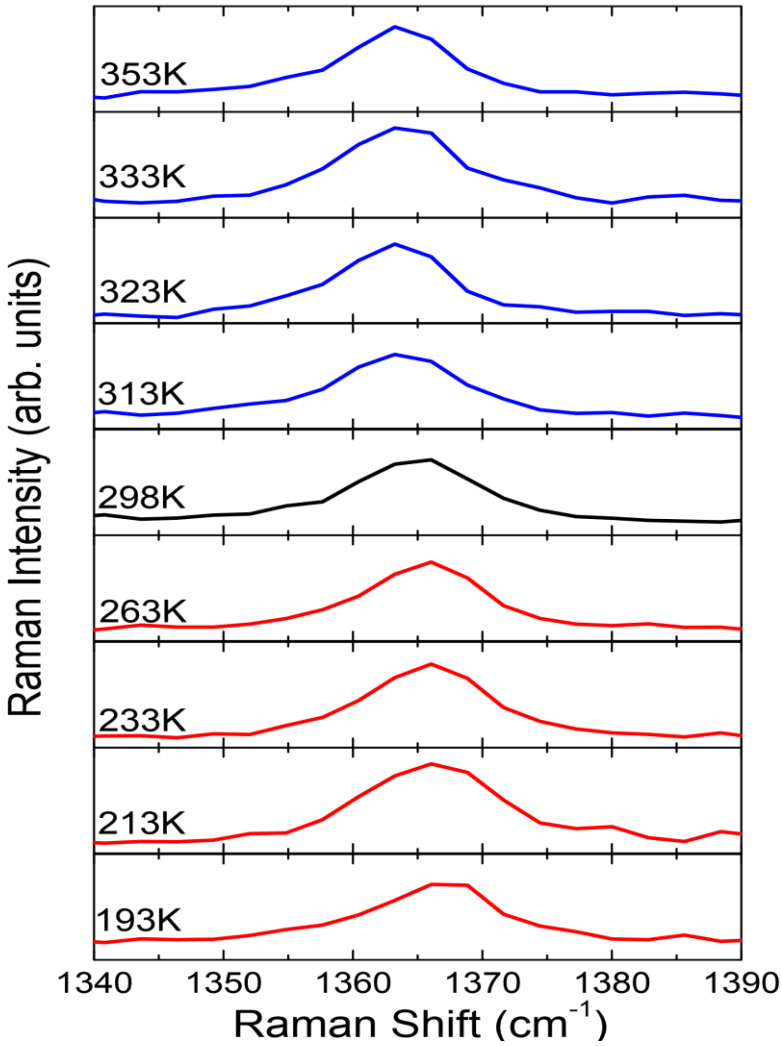

Figure SI-1. Raman spectra of monolayer *h*BN in the E_{2g} band frequency region for various temperatures.

2. Thermal Expansion Coefficients of Si, SiO_2 and *h*BN

In **Figure SI-2** the experimentally determined temperature dependence of the thermal expansion coefficients of bulk Si and SiO_2 is presented. Also, the calculated by means of the finite element method (FEM) TEC of a 90 nm thick SiO_2 in contact (on the top) with a bulk silicon (micrometer thickness), is shown in the temperature range 100–400 K. Furthermore, in **Figure SI-3** the TEC

from available experimental and theoretical works in the literature concerning 1-3 L and bulk *h*BN is presented. As it is evident, the temperature dependence of TEC for 1-3 L and bulk *h*BN is quite similar in the investigated temperature range (183–473 K).

For the temperature range examined herein, 183 K < T < 473 K, 1–3 L and bulk *h*BN exhibit small thermal expansion coefficient variations and the TEC maintains a negative value throughout. In the same temperature region silicon and Si/SiO_2 (90 nm) exhibit a positive TEC and stronger temperature dependence.

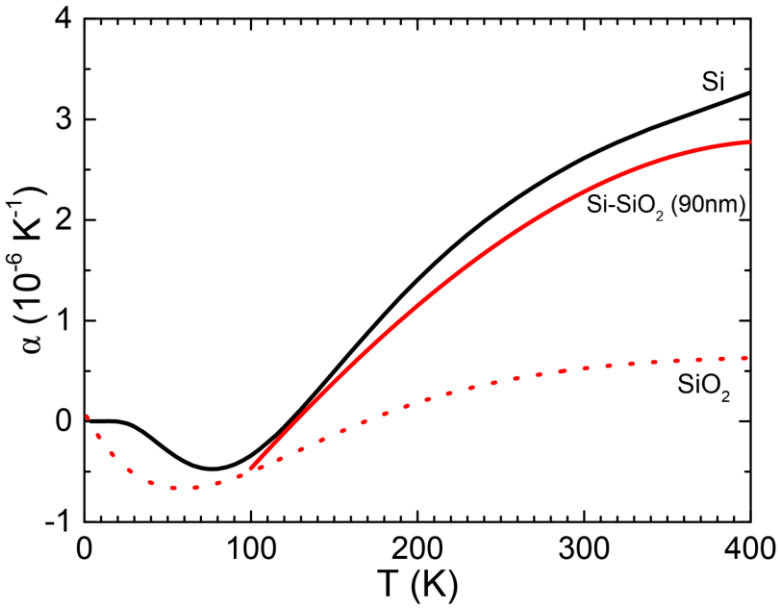

Figure SI-2. Experimental thermal expansion coefficients of crystalline Si (solid black line) and SiO_2 (dotted red line), in a wide temperature range. Data taken from Refs. [1-3]. The solid red line depicts the calculated thermal expansion coefficient of a 90 nm thick SiO_2 in contact with a micrometer thickness bulk silicon, in the temperature range 100–400 K.

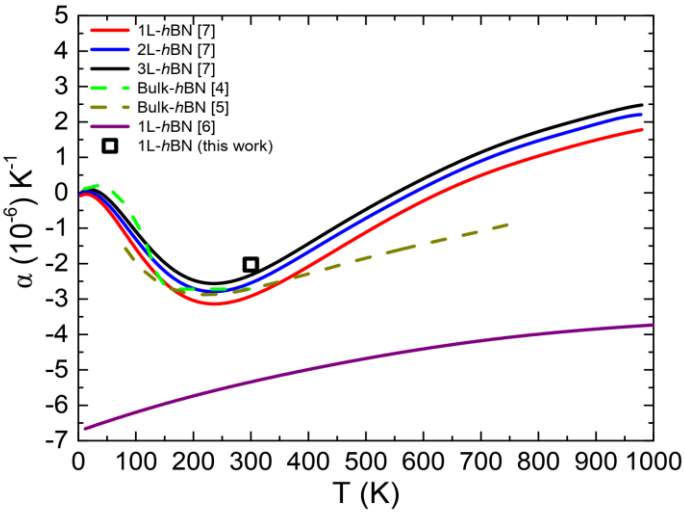

Figure SI-3. Thermal expansion coefficient of *h*BN for various thicknesses. Data taken from Refs. [4-7]. The black point is the estimated TEC of 1L *h*BN at room temperature.

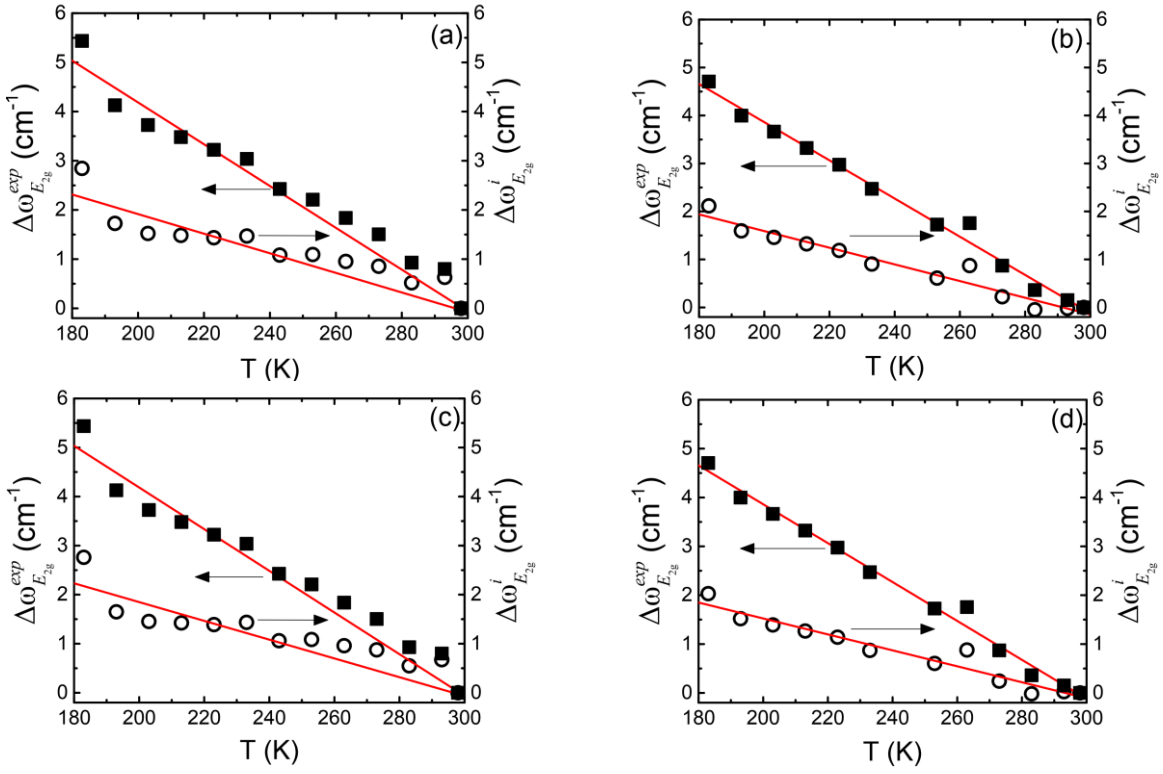

Figure SI-4. Extracted intrinsic temperature dependence $\Delta\omega^{i}_{E_{2g}}(T_m)$ of the E_{2g} phonon mode of freestanding monolayer *h*BN for the: (a), (c) examined ladder-like sample and (b), (d) an isolated

1L sample, derived as $\Delta\omega_{E_{2g}}^{exp}(T)-\Delta\omega_{E_{2g}}^{S}(T)$. In (a), (c) the theoretical TEC from ref [7] while for (b), (d) the experimental TEC from ref [4, 5] for bulk hBN is used.

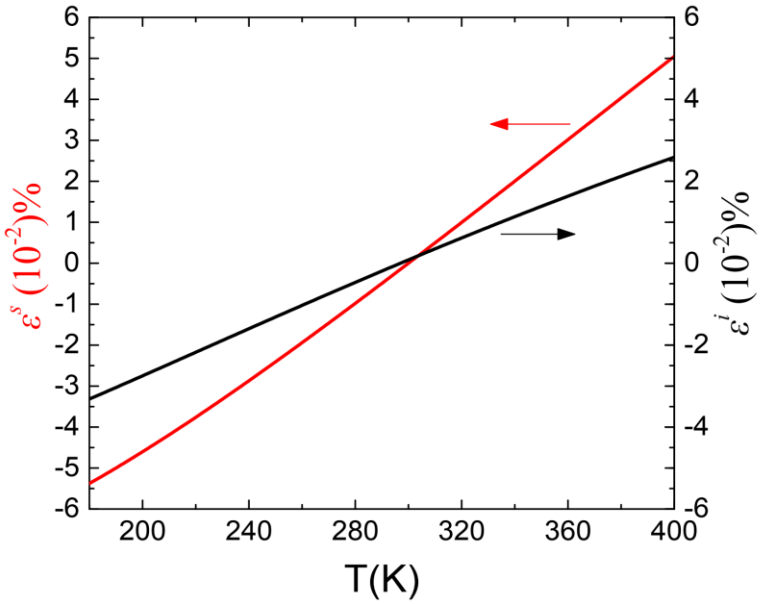

Figure SI-5. Thermal induced strain by TEC mismatch between monolayer *h*BN and the Si/SiO_2 (90 nm) substrate (ε^S, red line) and intrinsic strain (ε^i) of monolayer *h*BN (black line).

3. Finite Element Modeling

A 3D finite element model was developed to simulate the effect of temperature on the expansion of a Si/SiO_2 substrate, using the commercial code ANSYS [8]. Three-dimensional volume elements having 20 nodes and three degrees of freedom per node were utilized for both Si and SiO_2. Different mesh sizing was used in order to have computational accuracy and time efficiency. Additionally, in order to solve numerical issues in nano-FE modeling such, as incremental time steps, a scaled dimensional unit was used. The final element size and mesh was the result of compromise between computing time and accuracy.

Specifically, a mesh with 3nm element size was used in the volume of SiO_2 and the around volume of contact between Si and SiO_2, as shown in **Figure SI-6(a)**. For the rest of the structure, a coarser mesh was used with resize ratio 10, along to the thickness direction of Si volume, as

shown in **Figure SI-6(b)**. The model comprises over than 550.000 nodes and 130.000 elements. The model is constrained in all directions at the bottom nodes, as shown in **Figure SI-6(c)**.

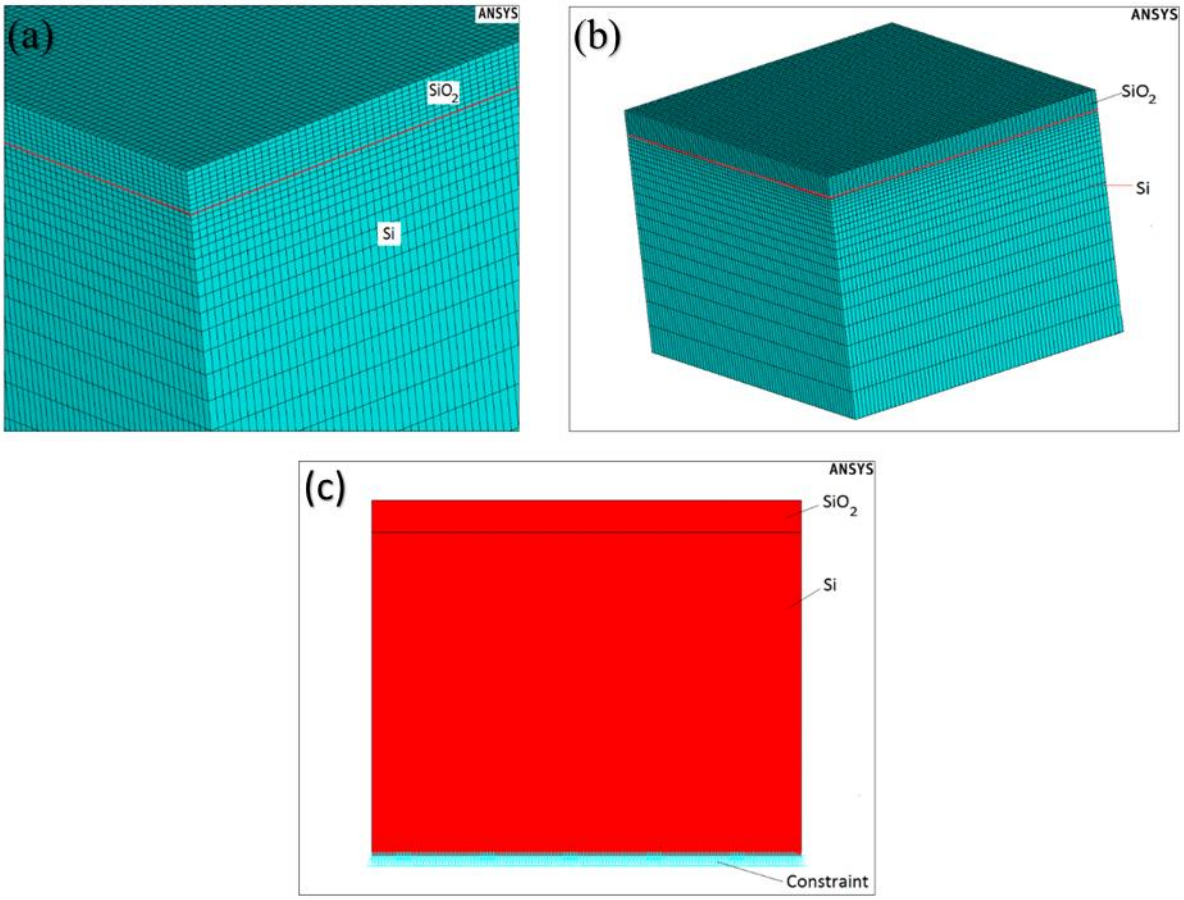

Figure SI-6. (a) Mesh of the volume of SiO_2 and the volume around contact between Si and SiO_2, (b) all model and (c) Constraint of the model.

A thermo-mechanical analysis was conducted using temperature dependent material properties. The temperature dependent material properties were inserted in the F.E code in a table form. The solution is generated in two basic steps. First a thermal analysis is performed and the results (temperature distribution) were input to the mechanical analysis in conjunction with the mechanical properties variation with temperature and the boundary conditions. An appropriate time-stepping scheme was used for analysis to achieve fast convergence of the solution and

reasonable accuracy. The mechanical analysis was performed using, a thermo-elasto-plastic material formulation employing the von Mises yield criterion [9, 10].

For the investigation square specimens were simulated with 4 μm length and 3μm thicknesses for Si and 60, 80, 90, 300 nm thicknesses for SiO_2. An example of the results from the F.E. model and the specimen size that was used for the analysis is presented following. Specifically, **Figure SI-7** show the distribution of the Displacement (**Figure SI-7(a)**) and the Total Mechanical and Thermal Strain (**Figure SI-7(b)**) for specimen of 3μm thicknesses Si and 60 nm thicknesses SiO_2 and the distribution of the Displacement (**Figure SI-7(c)**) and the Total Mechanical and Thermal Strain (**Figure SI-7(d))** for specimen of 4μm thicknesses Si and 300 nm thicknesses SiO_2, in case of thermal load of 240 ^oC.

The Mechanical Strain ε is expressed as the ratio of total deformation to the initial dimension of the material body in which the forces are being applied. In the F.E analysis the mechanical strain is computed as the change in length ΔL per unit of the initial distance of two nodes of the element and is defined as:

$$\varepsilon = \frac{\Delta L}{L_{in}} = \frac{L_f - L_{in}}{L_{in}} \tag{3.1}$$

where ε is the mechanical strain, L_{in} is the initial distance of two nodes of the element and L_f is the final distance.

Respectively, the Thermal Strain ε_{th} is defined as:

$$\varepsilon_{th} = \frac{\Delta L}{L_{in}} = \frac{L_f - L_{in}}{L_{in}} \tag{3.2}$$

where L_{in} is the distance of two nodes of the element before the change of temperature and L_f is after the change of temperature.

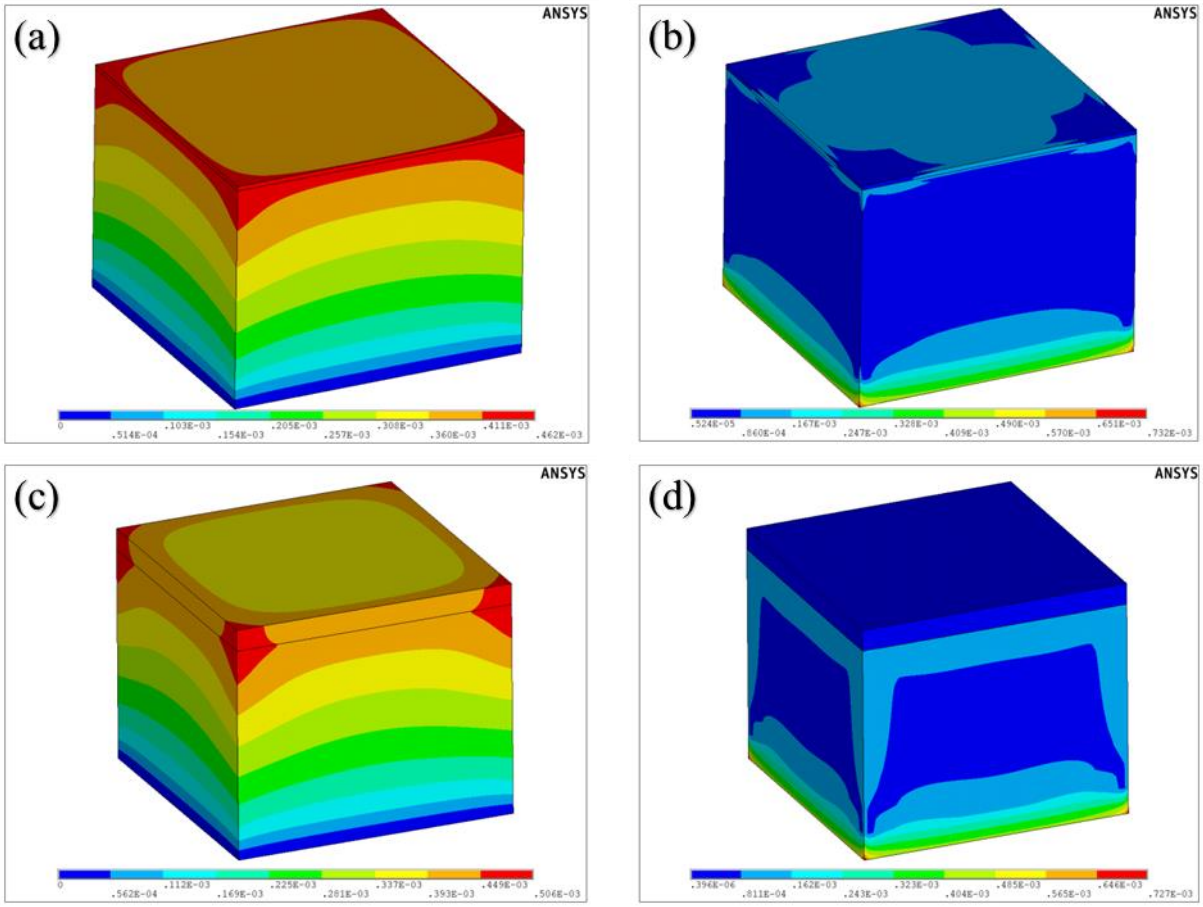

Figure SI-7. Example of Displacement and Total Thermal and Mechanical Strain distribution.

The Thermal Expansion α_L is related to temperature change by a coefficient of linear thermal expansion due to change distance of two nodes of the element per degree of temperature change, namely:

$$a_L = \frac{1}{L_{in}} \frac{\Delta L}{\Delta T} \quad \text{or} \quad a_L = \frac{\Delta L}{L_{in}} \frac{1}{\Delta T} \tag{3.3}$$

where $\Delta T = T_f - T_{in}$, with T_{in} the initial temperature and T_f the final temperature.

Finally, the Thermal Expansion is a linear coefficient of a material relating the rate at which strain changes with respect to a unit change in temperature and can be estimated by:

$$\varepsilon_{th} = a_L \Delta T \tag{3.4}$$

In case of a construction with more than one material, the strain is the combination of the thermal strain of all materials and the mechanical strain due to the forces between the contact areas of materials.

4. Interference effects on the Raman spectrum of *h*BN

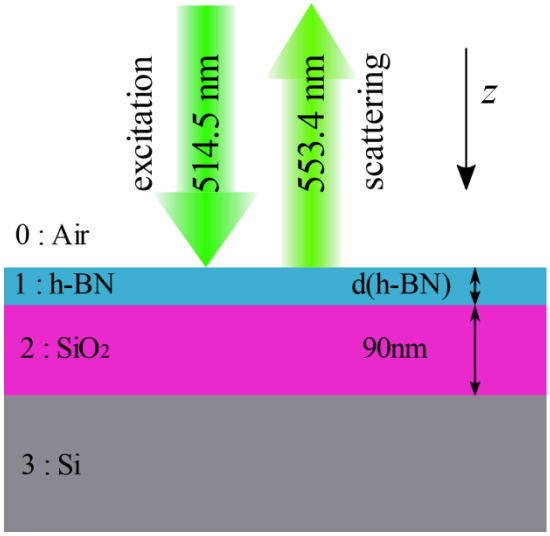

Figure SI-8. The geometry of the system.

The total Raman signal from the *h*BN crystal is

$$I_{Raman} \propto \int_{z=0}^{d} \left| E_{exc}(z) E_{sc}(z) \right|^2 dz \tag{4.1}$$

where $E_{exc}(z)$, $E_{sc}(z)$ are the electric field amplitude, at depth z from the upper surface of the *h*BN crystal, of the exciting and scattered radiation, respectively, and d is the *h*BN crystal's thickness. The contribution of the n^{th} layer to the total Raman signal, $I(n)$, is

$$I(n) = \int_{(n-1)d_{1L}}^{nd_{1L}} f(z) dz = \left\langle f(z) \right\rangle_n d_{1L} \ , \ n = 1, 2, 3, \ldots \tag{4.2}$$

where, $f(z) = \left| E_{exc}(z) E_{sc}(z) \right|^2$, d_{1L} is the thickness of single layer *h*BN (≈0.333 nm) and $\left\langle f(z) \right\rangle_n$ is the mean value of $f(z)$ in the integration interval. Since this interval is very small compared to

the wavelength of the radiation used, $\frac{d_{1L}}{\lambda} \approx 10^{-3}$, the integrand $(f(z))$ can be sufficiently approximated up to first order in z. Consequently, the average value is $\langle f(z) \rangle_n \approx f\left[(n-\frac{1}{2})d_{1L}\right]$. Finally,

$$I(\mathrm{n}) \propto f\left[(n-\frac{1}{2})d_{1L}\right] \tag{4.3}$$

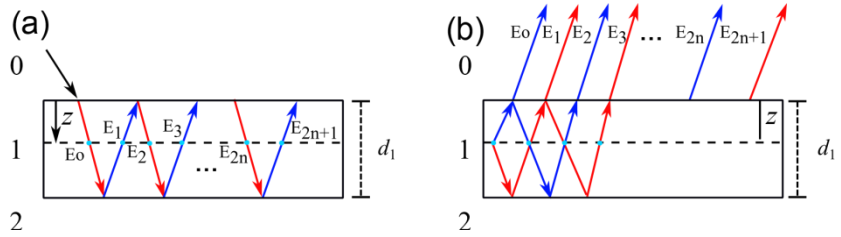

Figure SI-9. Calculation of the total electric field of (a) the exciting radiation and (b) the scattered radiation inside a slab.

The calculation of $E_{exc}(z)$ can be realized by considering the geometry shown in **Figure SI-9**. A thin slab of a material (*h*BN in our case) separates two semispaces of different materials. Each material is indexed from 0 (air) to 2 (SiO_2/Si). A beam of light is incident on the 0-1 interface and is partially transmitted inside the slab. The transmitted beam propagates across the slab's thickness until it strikes the 1-2 interface where reflection occurs. This reflected beam travels upwards until it reaches the 1-0 interface. The reflections occurring in the slab result in an infinite number of downwards and upwards propagating beams. The total electric field amplitude $E_{exc}(z)$ is calculated by summing the amplitudes of all the multiply reflected beams. The refractive index of the materials involved are $n_i(\lambda), i = 1,2,3$ and the thickness of slab 1 is d_1. Considering that the Fresnel reflection and transmission coefficients for the electric field amplitude at the interface

between *i-j* mediums (propagating from *i* to *j*) are $r_{ij} = \frac{n_i - n_j}{n_i + n_j}$ and $t_{ij} = \frac{2n_i}{n_i + n_j}$, respectively, $E_{exc}(z)$ is

$$E_{exc}(z) = \frac{E_0(z) + E_1(z)}{1 + r_{01} r_{12} \exp(-2i\phi_1)} \tag{4.4}$$

where, $\phi_1 = \frac{2\pi n_1 d_1}{\lambda_{exc}}$, $E_0(z) = \mathrm{t}_{01} \exp\left(-\frac{2i\pi n_i}{\lambda_{exc}} z\right)$ and $E_1 = \mathrm{t}_{01}\mathrm{r}_{01}\exp(-2\mathrm{i}\phi)\exp\left(-\frac{2i\pi n_i}{\lambda_{exc}} z\right)$. In this case, λ_{exc} is the exciting radiation wavelength. Also, the refractive indexes of the materials depend on the wavelength and the corresponding values must be used. It must be noted that r_{12} in equation (7.4) is the effective reflection coefficient r_{eff} of the *h*BN-SiO_2-Si stack. This can be calculated by using again the multiple beam interference concepts [11]. After performing the summation of the amplitudes r_{eff} is found equal to

$$r_{12} \equiv r_{eff} = \frac{r_{ab} + r_{bc} \exp(-2i\phi_b)}{1 + r_{ab} r_{bc} \exp(-2i\phi_b)} \tag{4.5}$$

where the a, b, c indices refer to the *h*BN, SiO_2, and Si. The phase factor now is $\phi_b = \frac{2\pi n_b d_b}{\lambda_{exc}}$.

Similarly, the amplitude $E_{sc}(z)$ can be calculated based on the scheme shown in **Figure SI-9(b)**. Interestingly, the results are obtained by changing $t_{01} \rightarrow t_{10}$ in equation (7.4), in addition to using the proper wavelength and refractive indices. For very thick BN crystals the Raman signal intensity at depth z can be calculated by considering only the absorption of the incident and scattered radiation. As such, the contribution to the total Raman signal from scattering at depth z, $I(z)$, is

$$I(z) \propto \exp\left(-\frac{z}{\delta_{exc}}\right)\exp\left(-\frac{z}{\delta_{sc}}\right) = \exp\left(-\frac{z}{L}\right) \tag{4.6}$$

The reduced scattering length L is connected to the penetration depths at excitation (514.5 nm) and scattering (553.4 nm) wavelengths, δ_{exc} and δ_{sc} respectively, by the formula

$$\frac{1}{L} = \frac{1}{\delta_{exc}} + \frac{1}{\delta_{sc}} \tag{4.7}$$

According to the data used for the refractive index of BN [12], we find that the refractive indexes are (1.582–0.22j) and (1.592–0.21j) at 514.5 nm and 553.4 nm, respectively, corresponding to penetration depths 186.1 nm and 209.3 nm, respectively. As such *L* is calculated equal to 98.5 nm. Fitting an exponential decay function to the calculated Raman signal vs depth curve in **Figure SI-10(f)** in the manuscript it is indeed found that the decay constant is 98.5 nm. Since the graphs in **Figure SI-10(f)** were calculated by considering interference effects explicitly, the correctness of the model presented here is verified.

5. Calculated depth dependent Raman Intensities for *h*BN of various thicknesses

In **Figure SI-10(a)-(f)**, the calculated Raman intensity as a function of depth from the air/*h*BN interface is presented (black lines) for *h*BN crystals of various thicknesses. In the theoretical analysis, regarding the interference effect on Raman response of 2D materials (see section 4) normal incidence of the incident beam is considered, which is a common practice in relevant works, since this approximation captures the experimental results sufficiently well [13]. For small thicknesses (1 and 11 layers) the intensity is uniform throughout the crystal as shown in **Figure SI-10(a)** and **(b)**. For thicker crystals, the intensity distributions are non-trivial. In **Figure SI-10(c)** it is evident that for a 120-layer thick BN crystal, the bottom half of the crystal (close to the BN/SiO_2 interface) contributes more to Raman signal than the upper half. For 400 layers (**Figure SI-10(d)**), only the top and bottom quarters of the crystal contribute to the Raman signal with the

middle part's contribution being almost zero. For 1400 layers, the intensity distribution approaches that of an exponential decay with slightly visible undulations (**Figure SI-10(e)**). The expected exponential decay law is fully recovered only for very thick crystals (a few thousand layers) as can be seen in **Figure SI-10(f)**.

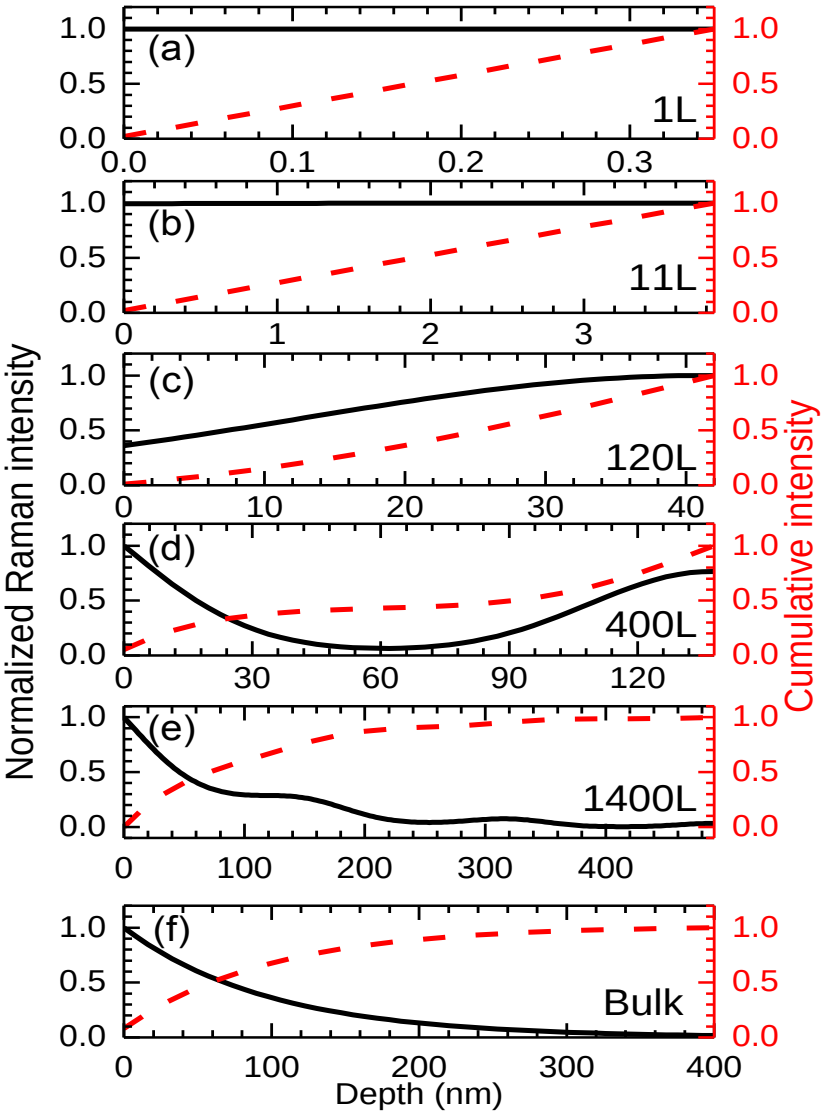

Figure SI-10. Calculated Raman intensities (black solid lines) and cumulative Raman intensities (red dash lines) as functions of depth inside the *h*BN crystal for thicknesses of :(a) 0.35 layer (1L), (b) 3.85nm (11L), (c) 42nm (120L), (d) 140nm (400L), (e) 470 nm (1400L) and (e) bulk (8000 layers). The depth is measured from the air/hBN interface.

It is noted that for very thick BN crystals, the Raman signal follows an exponential decay $I \propto \exp\left(-\frac{z}{L}\right)$ with a scattering length L = 98.5 nm. This value is extracted using the optical constants of *h*BN found in Ref. [12]. According to the data presented in Refs. [14] and [15] the scattering length is roughly 250 nm for 2.41 eV excitation energy. Moreover, the cumulative Raman intensity for the aforementioned cases are presented (red dash lines) in **Figure SI-10(a)-(f)**. From these plots we can conclude that for the 120 (400) layers the 50% of the collected Raman scattering intensity comes from 40% (35%) of the total slab thickness with reference the *h*BN/SiO_2 interface. These observations point out that interference effects can have a significant impact on the Raman spectrum of *h*BN even for crystals much thicker than the Raman penetration depth.

6. Estimation of interlayer strain transfer efficiency factor and intrinsic temperature shift of the E_{2g} mode of freestanding 11L *h*BN

It was reported [16, 17] that the rate of change of the E_{2g} band position with applied strain is linearly related to the Young modulus, E, namely, $E \propto {\partial\omega_{E_{2g}}^{\exp}}/{\partial\varepsilon}$. Gong *et al*. [18] developed a model to evaluate the strain transfer efficiency between the adjacent layers of multilayer graphene based on past analysis of Zalamea *et al.* [19] for multiwall carbon nanotubes. The degree of strain transfer efficiency is described by the parameter k. The measured value of the slope for the 11L is related to the slope for monolayer, the number of layers, N and the k parameter via the equation (6.1)

$$ {\partial\omega_{E_{2g}}^{\exp,11L}}/{\partial\varepsilon} = \frac{{\partial\omega_{E_{2g}}^{\exp,1L}}/{\partial\varepsilon}}{\left[N - k(N-1)\right]} \qquad (6.1) $$

It should be stressed that for k=0 equation (4.1) gives $\partial\omega_{E_{2g}}^{\exp,11L}/\partial\varepsilon = \dfrac{\partial\omega_{E_{2g}}^{\exp,1L}/\partial\varepsilon}{N}$ which is equal to the statement that $E^{11L} = \dfrac{E^{1L}}{N}$ [18]. Also, for k=1 (perfect strain transfer) the slopes for 11L and 1L are the same. From reference [20] the E_{2g} mode Grüneisen parameter, $\gamma_{E_{2g}}$, for the 1L and the multilayer (~10L) are about 1.8 and 1, respectively. Since the E_{2g} mode frequency position of the monolayer and 11L layer crystal are similar, equation (6.1) gives

$$\frac{\gamma_{E_{2g}}^{1L}}{\gamma_{E_{2g}}^{11L}} = \frac{\partial\omega_{E_{2g}}^{1L}/\partial\varepsilon}{\partial\omega_{E_{2g}}^{11L}/\partial\varepsilon} \tag{6.2}$$

From (6.1), (6.2) and for N=11 a strain transfer efficiency factor k of 0.92 can be obtained. Furthermore, we can easily calculate a mean $\partial\varepsilon^S/\partial T$ for the 11L, considering that the first layer adhered to the substrate experience strain ε^S due to the TEC mismatch. Then, the second layer experience strain $k\cdot\varepsilon^S$, the third $k^2\cdot\varepsilon^S$ and a geometric sequence is formed up to the 11th layer. Consequently, we can write

$$\frac{\partial\varepsilon^{11L,S}}{\partial T} = \frac{\partial\varepsilon^{1L,S}}{\partial T}\cdot\frac{1}{11}\frac{k^{11}-1}{k-1} = 0.682\cdot\frac{\partial\varepsilon^{1L,S}}{\partial T} \tag{6.3}$$

Therefore, by this crude model we can extract the intrinsic temperature shift of the E_{2g} mode of freestanding 11L hBN by subtracting the experimental value (-0.0318 cm^{-1}/K) from the TEC mismatch with the substrate ($\beta\cdot 0.682\cdot\partial\varepsilon^{1L,S}/\partial T$) which is -0.0155 cm^{-1}/K.

7. Temperature dependence of the FWHM of the E_{2g} mode for *h*BN of various thicknesses

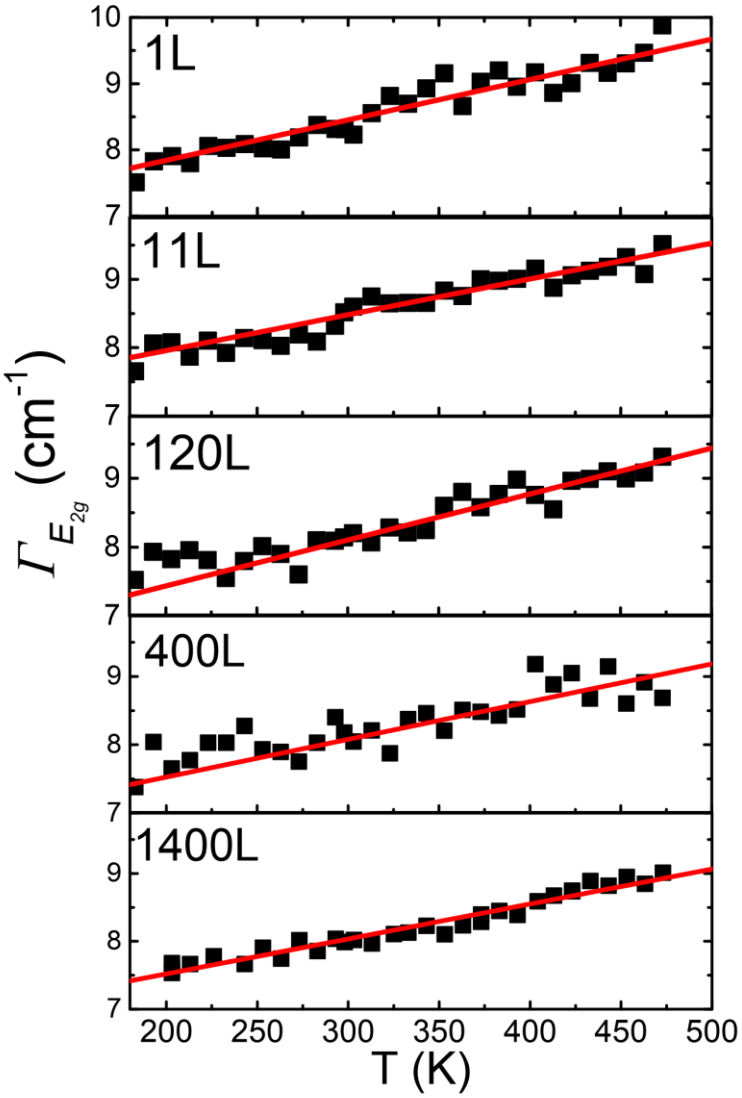

Figure SI-11. Temperature dependence of the full width at half maximum ($\Gamma_{E_{2g}}$) of the E_{2g} mode for *h*BN of various thicknesses.

Table SI-1. Temperature dependence of FWHM of the E_{2g} phonon mode for different sampling points positioning on regions with various thicknesses ranging from monolayer to bulk boron nitride. The data are fitted by $\Gamma_{E_{2g}} = \Gamma_o + \chi \cdot T$, where Γ_o is the FWHM of the E_{2g} phonon mode at 0 K and χ is the slope of the dependence FWHM *vs T*.

Region	Thickness (nm)	Number of layers	Γ_o (cm^{-1}) T< 305 K	χ (cm^{-1}/K) T> 305 K
Bulk hBN	466.5	1400	6.5(1)	0.0052(4)
	137.9	400	6.4(3)	0.0050(7)
	41.9	120	6.3(2)	0.0059(4)
FL-hBN	3.9	11	6.9(1)	0.0053(4)
1L-hBN	0.4	1	6.5(3)	0.0065(5)
			6.9(5)*	0.0067(4)**

* T<350K, ** T>350K (isolated individual monolayer sample)

8. Anharmonic effects on the temperature dependence of the E_{2g} mode of bulk *h*BN

Using the analysis presented in Balkanski *et al.* [21-23] the temperature dependence of the E_{2g} frequency position and full width at half maximum of bulk *h*BN (1400L) in the examined range (203 K < *T* < 850 K) is analyzed considering three-phonon and four-phonon interactions. The $\Delta\omega(T)$ and $\Gamma(T)$ of the Raman active E_{2g} mode can be fitted with the following expressions:

$$\Delta\omega(T) = A\left[1+\frac{2}{e^x-1}\right] + B\left[1+\frac{3}{e^y-1}+\frac{3}{(e^y-1)^2}\right] \quad (8.1)$$

$$\Gamma(T) = C\left[1+\frac{2}{e^x-1}\right] + D\left[1+\frac{3}{e^y-1}+\frac{3}{(e^y-1)^2}\right] \quad (8.2)$$

where $x = \frac{\hbar\omega}{2kT}$, $y = \frac{\hbar\omega}{3kT}$ and the coefficients *A (C)* and *B (D)* are constants, representing the contributions of three-phonon and four-phonon processes to the frequency shift (FWHM), respectively. The fitting of both the frequency shift and FWHM of the E_{2g} phonon mode with temperature using the equations (8.1) and (8.2) is given by the solid red curve in **Figures SI-12(a)**, **(b)**. The agreement between the calculated curve and the experimental data is excellent and the best values of the fitting parameters are –10.4 cm^{-1}, –1.49 cm^{-1} for *A* and *B* (equation (8.1)) and 3.27 cm^{-1}, 0.42 cm^{-1} for *C* and *D* (equation (8.2)). The dashed curve corresponds to the theoretical fitting accounting only for three-phonon processes.

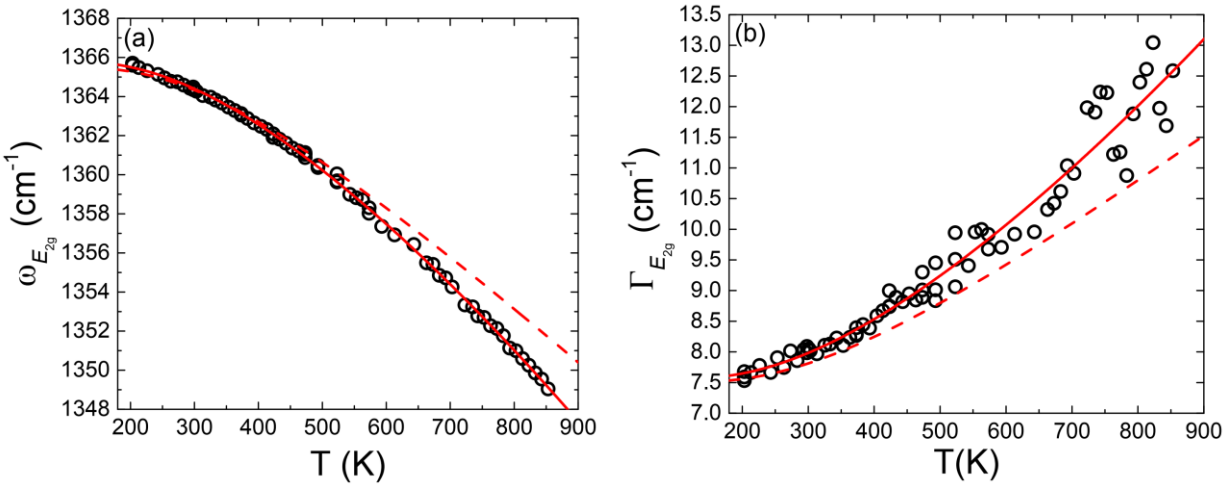

Figure SI-12. Temperature dependence of the E_{2g}: (a) Raman peak frequency and (b) FWHM, ($\Gamma_{E_{2g}}$) (empty circles). The solid (dashed) lines depict the contribution of both three-phonon and four-phonon (three-phonon only) decay processes.

9. *k*-space velocity autocorrelation function via molecular dynamics

The used code implements a method that makes use of atomic trajectories and velocities to form the *k*-space velocity autocorrelation function (*k*VACS) and compute frequencies of vibrational modes at *finite* temperatures [24]. To acquire the phonon frequencies ω that correspond to a given

wavevector $\boldsymbol{k}$ we consider the velocity distribution in reciprocal space that is obtained by the spatial Fourier transform

$$v_k^p(t) = \sum_j v_j^p(t) e^{-i\mathbf{k}\cdot\mathbf{R}_j(t)} \tag{9.1}$$

where j sums over unit cells (once for each particular atom of the crystal basis, $\mathbf{R}_j(t)$ are the position vectors of the corresponding atoms) and p is a component (x, y, or z) in a Cartesian coordinate system (i.e. $v_j^p(t)$ is the p-component of the velocity of the atom j at position $\mathbf{R}_j(t)$. The power spectral density (PSD) is given by the spectral decomposition of the k-space velocity autocorrelation function (kVACF) $Z_k^p(t)$, namely

$$Z_k^p(t) = \frac{\left\langle v_k^p(0) v_k^{*p}(t) \right\rangle}{\sum_{p'} \left\langle v_k^{p'}(0) v_k^{*p'}(0) \right\rangle} \tag{9.2}$$

where averages are obtained over different initial times during the simulation. Once the PSD is calculated via the temporal Fourier transform of the kVACF, the phonon frequencies corresponding to the wavevector $\boldsymbol{k}$ are obtained by identifying the peaks in the PSD.

10. References

1. Watanabe, H.; Yamada, N.; Okaji, M. Linear Thermal Expansion Coefficient of Silicon from 293 to 1000 K. *International Journal of Thermophysics* **2004,** *25* (1), 221-236.
2. Okada, Y.; Tokumaru, Y. Precise determination of lattice parameter and thermal expansion coefficient of silicon between 300 and 1500 K. *Journal of Applied Physics* **1984,** *56* (2), 314-320.
3. Hahn, T. A.; Kirby, R. K. Standard Reference Material 739. In *Fused-Silica Thermal Expansion*, National Institute of Standards and Technology: Gaithersburg, Maryland, 1991.
4. Yates, B.; Overy, M. J.; Pirgon, O. The anisotropic thermal expansion of boron nitride. *Philosophical Magazine* **1975,** *32* (4), 847-857.
5. Paszkowicz, W.; Pelka, J. B.; Knapp, M.; Szyszko, T.; Podsiadlo, S. Lattice parameters and anisotropic thermal expansion of hexagonal boron nitride in the 10–297.5 K temperature range. *Applied Physics A* **2002,** *75* (3), 431-435.
6. Anees, P.; Valsakumar, M. C.; Panigrahi, B. K. Effect of strong phonon-phonon coupling on the temperature dependent structural stability and frequency shift of 2D hexagonal boron nitride. *Physical Chemistry Chemical Physics* **2016,** *18* (4), 2672-2681.
7. Cai, Q.; Scullion, D.; Gan, W.; Falin, A.; Zhang, S.; Watanabe, K.; Taniguchi, T.; Chen, Y.; Santos, E. J. G.; Li, L. H. High thermal conductivity of high-quality monolayer boron nitride and its thermal expansion. *Sci Adv* **2019,** *5* (6), eaav0129.
8. *ANSYS: User's manual*, version 17.2; software for technical computation; Swanson Analysis Systems Inc.: Houston, 2016.
9. Lewis, R. W.; Morgan, K.; Thomas, H. R.; Seetharamu, K. N. *The Finite element method in heat transfer analysis*. Wiley: Chichester, 1996.
10. Bathe, K.-J. *Finite element procedures in engineering analysis*. Prentice-Hall: Englewood Cliffs ; London, 1982.
11. Lecaruyer, P.; Maillart, E.; Canva, M.; Rolland, J. Generalization of the Rouard method to an absorbing thin-film stack and application to surface plasmon resonance. *Appl. Opt.* **2006,** *45* (33), 8419-8423.
12. Doll, G. L. - Boron Nitride (BN). In *Handbook of Optical Constants of Solids*, Palik, E. D., Ed. Academic Press: Burlington, 1997; pp 425-443.
13. Yoon, D.; Moon, H.; Son, Y.-W.; Choi, J. S.; Park, B. H.; Cha, Y. H.; Kim, Y. D.; Cheong, H. Interference effect on Raman spectrum of graphene on SiO_2/Si. *Physical Review B* **2009,** *80* (12), 125422.
14. Hoffman, D. M.; Doll, G. L.; Eklund, P. C. Optical properties of pyrolytic boron nitride in the energy range 0.05---10 eV. *Physical Review B* **1984,** *30* (10), 6051-6056.
15. Reich, S.; Ferrari, A. C.; Arenal, R.; Loiseau, A.; Bello, I.; Robertson, J. Resonant Raman scattering in cubic and hexagonal boron nitride. *Physical Review B* **2005,** *71* (20), 205201.
16. Frank, O.; Tsoukleri, G.; Riaz, I.; Papagelis, K.; Parthenios, J.; Ferrari, A. C.; Geim, A. K.; Novoselov, K. S.; Galiotis, C. Development of a universal stress sensor for graphene and carbon fibres. *Nature Communications* **2011,** *2* (1), 255.
17. Huang, Y.; Young, R. J. Effect of fibre microstructure upon the modulus of PAN- and pitch-based carbon fibres. *Carbon* **1995,** *33* (2), 97-107.
18. Gong, L.; Young, R. J.; Kinloch, I. A.; Riaz, I.; Jalil, R.; Novoselov, K. S. Optimizing the Reinforcement of Polymer-Based Nanocomposites by Graphene. *ACS Nano* **2012,** *6* (3), 2086-2095.

19. Zalamea, L.; Kim, H.; Pipes, R. B. Stress transfer in multi-walled carbon nanotubes. *Composites Science and Technology* **2007,** *67* (15), 3425-3433.
20. Androulidakis, C.; Koukaras, E. N.; Poss, M.; Papagelis, K.; Galiotis, C.; Tawfick, S. Strained hexagonal boron nitride: Phonon shift and Grüneisen parameter. *Physical Review B* **2018,** *97* (24), 241414.
21. Balkanski, M.; Wallis, R. F. Haro, E. Anharmonic effects in light scattering due to optical phonons in silicon. *Physical Review B* **1983,** *28* (4), 1928-1934.
22. Klemens, P. G. Anharmonic Decay of Optical Phonons. *Phys Rev* **1966,** *148* (2), 845-&.
23. Zouboulis, E. S.; Grimsditch, M. Raman scattering in diamond up to 1900 K. *Phys Rev B Condens Matter* **1991,** *43* (15), 12490-12493.
24. Koukaras, E. N.; Kalosakas, G.; Galiotis, C.; Papagelis, K. Phonon properties of graphene derived from molecular dynamics simulations. *Scientific Reports* **2015,** *5*, 12923.